RESEARCH   **Open Access**

Review of Several Experimental Methods for Characterization of Micro- and Nano-Scale Pores in Cement-Based Material

Abudushalamu Aili[1*] and Ippei Maruyama[1,2]

Abstract

Mechanical properties and durability of cement-based materials are largely affected by pore structures. This paper provides an overview of several experimental techniques to characterize pore size distribution and specific surface area, with focus on pores in calcium silicate hydrates. The reviewed experimental techniques are nitrogen and water vapor sorption isotherm, proton nuclear magnetic resonance (^{1}H-NMR) and small-angle scattering (SAS). Different pretreatment methods are compared for sorption measurements. Pore size distribution and specific surface area are analyzed using data from different methods to understand difference and consistency of these methods. It is found that pore size distribution calculated from sorption isotherm is very sensitive to adsorption model. Though specific surface areas from different techniques are quite different from each other, they are all able to detect the microstructural alteration due to long-term drying.

Keywords: cement, pore size distribution, specific surface area, sorption isotherm, ^{1}H-NMR, SAS

1 Introduction

Cement paste and concrete are porous material composed from solid skeleton and pores, with the size of pores varying from several micrometers to nanometers. These pores are of great importance for not only mechanical properties but also for durability of cement-based materials. Most of the chemical agents, that are triggers of degradation, invade into the material through pores. Chemical reactions then takes place inside the pores, causing different results based on the size of the pores. For instance, during salt attack in cement paste, crystallization pressure is different in larger pores and smaller pores (Scherer 1999, 2004). It was confirmed in Sasano et al. (2018) that drying shrinkage reduced the performance of reinforced concrete structure. This drying shrinkage is caused by three different mechanisms in

different pores at different relative humidities (Hansen 1987). In larger pores at higher relative humidity, capillary pressure causes the drying shrinkage (Feldman and Sereda 1970; Powers 1965, 1968). When relative humidity continues to decrease, disjoining pressures of water in smaller pores play main role (Bazant 1972; Wittmann 1973); whereas, at even lower relative humidity in much smaller pores, the shrinkage is caused by surface energy (Feldman and Sereda 1964; Powers 1965). Therefore, characterizing pore size and pores structure is necessary to better estimate the durability of cementitious materials and has been a topic of many studies since decades. This article aims at reviewing such experimental techniques and related theories that are widely used on Ordinary Portland Cement (OPC) pastes. Blended cement pastes will not be considered specifically, but the experimental techniques and theories remain the same as OPC pastes.
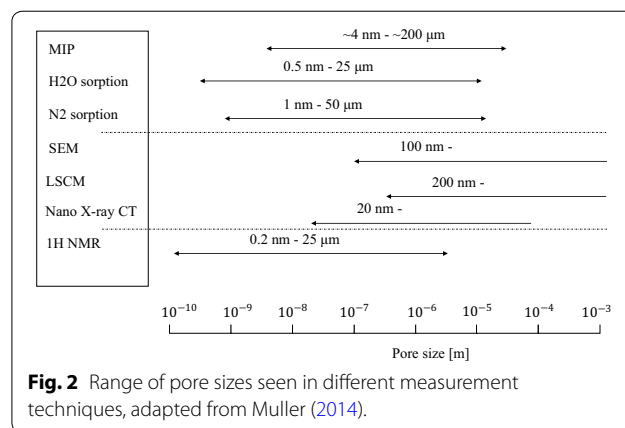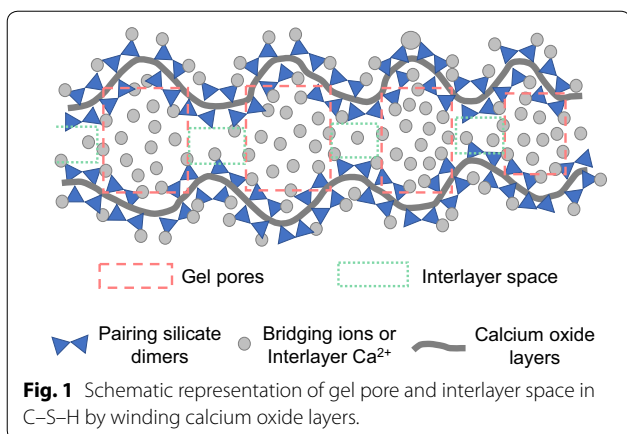
Ordinary cement paste is a multi-phase material, composed from unhydrated clinker and hydration products. The hydration products include crystalline phases such as Portlandite, sulfoaluminates and amorphous calcium

*Correspondence: aili.abudushalamu@d.mbox.nagoya-u.ac.jp
[1] Graduate School of Environmental Engineering, Nagoya University, Furocho, Chikusa-ku, Nagoya 461-8603, Aichi, Japan
Full list of author information is available at the end of the article

Fig. 1 Schematic representation of gel pore and interlayer space in C–S–H by winding calcium oxide layers.

Fig. 2 Range of pore sizes seen in different measurement techniques, adapted from Muller (2014).

silicate hydrate (C–S–H). During hydration, calcium oxide and silicate from clinker dissolve into water. Calcium oxides forms layers on which silicates will be paired in the form of dimers (see Fig. 1). Two pairing dimers next to each other can be connected via the bridging position, which can be occupied by silica or aluminum or calcium ions. However, some of the bridging positions are empty or cannot be connected to the next bridging position. Hence, calcium ions can be more concentrated in some places than others, causing more water in these places. As a result, calcium oxide layers will be winded, forming larger spaces between them in some place and smaller spaces in other (Gartner et al. 2017). These larger spaces are called gel pores, while the smaller spaces are known as interlayer space, as shown Fig. 1. Though different from the models in Geng et al. (2017; Richardson 2004) which attribute the gel pores to the imperfect growth of calcium silicate layers, they all suggest that both gel pores and interlayer space are inside of C–S–H, and connected to each other. The connection between gel pores and interlayer spaces is also confirmed by $T_2 - T_2$ correlation of gel pores and interlayer spaces in 2D proton nuclear magnetic resonance relaxometry (Mcdonald et al. 2007; Valori et al. 2010). Said otherwise, the calcium silicate layers, interlayer water and gel space form together the C–S–H gel. Due to the small number of repeating unit in the calcium silicate layer, experimental techniques for crystallography such as X-ray diffraction cannot be used to study the structure of the C–S–H that appears amorphous. However, it is possible to observe that calcium silica layers are crystal-based structure by transmission electron microscope (TEM), where comes the name of C–S–H nanocrystalline (Richardson 1999). According to Jennings (2000), the size of the interlayer space between calcium silica layers is around 0.1 nm–1 nm; whereas, the size of gel pores are 2 nm–10 nm. On the contrary, Mehta and Monteiro (2006) named all pore spaces in C–S–H gel

as interlayer space. Outside of the C–S–H gel, the cement paste contains also capillary pores whose size varies from 10 µm to 10 nm. Capillary pores result from consumption of water during hydration and locate between hydrates and clinkers. Recently, based on relaxation times measured by proton nuclear magnetic resonance relaxometry (^{1}H-NMR), Muller et al. (2013) classified pores into four types: interlayer space, gel pores, interhydrate pores and capillary pores. Among them, interlayer space and gel pores are confined by C–S–H layers. Since most long-term durability issues originate from C–S–H, experimental methods to review in this work are selected with an objective to study gel pores and interlayer spaces of C–S–H.

Many experimental techniques have been used to characterize the pore structure of cementitious materials, including direct methods, in which pore structure is observed by imaging techniques, and indirect methods, in which some probe is used to get information about the pore structure. The range of measurable pore size of each method is limited to only a part of the full pore structure of cement paste. Figure 2 resumes the approximate range of pore size of several different methods.

In direct methods, pore structure is analyzed from 2D or 3D images of samples. The key factor of the image-based methods is the size of a pixel/voxel, which limits the range of pore size. Smaller pixel/voxel size permits access to smaller pores, but limits, on the other hand, the size of total observation area; hence, representativity of the measurement would be lower. In one of the pioneer works, 2D images of Scanning Electron Microscopy (SEM) with pixel size around 0.5 µm (Lange et al. 1994; Scrivener 1989, 2004) were used to estimate total porosity, pore size distribution. Comparing to 2D image of SEM, 3D images provides more topological information on pore network. For instance, Lanzón et al. (2012) used X-ray microtomography to analyze the 3D pore structure

of mortar while 3D microstructure of cement paste was obtained by X-ray microtomography and X-ray nanotomography in Bossa et al. (2015). Laser scanning confocal microscopy (LSCM) can be combined with serial sectioning to analyze influence of 3D pore structure of cement paste (Yio et al. 2015, 2019). It is also possible to reconstruct 3D image combining the SEM with Focused Ion Beam (FIB) (Holzer et al. 2004). Although the size and shape of the pores can be observed directly with these methods, sophisticated image analysis algorithms are necessary to quantify the pore structure.

Among the indirect methods, there are experimental techniques in which a substance is introduced as probe into the sample to measure the pore size and volume, such as Mercury Intrusion Porosimetry (MIP) and gas/vapor adsorption techniques. MIP is one of the widely used techniques to measure pores structure of cementitious materials (Van Brakel et al. 1981; Muller and Scrivener 2017). MIP was applied on concrete for the first time in 1961 (Edel'man and Sominskii 1961). In MIP, sample is dried prior to the test and then mercury is forced into the pores of the material, with step-by-step increasing pressure. The experimental relation between applied pressure and volume of introduced mercury is then used to infer pore size distribution based on Laplace Equation/Washburn Equation (see Eq. (5)). MIP is known as a destructive method (Diamond 2000) and recently, using X-ray CT image analysis, Wang et al. (2019) quantified the damage caused by MIP. In addition, pretreatment disturbs the pore structure and measurement results of MIP are affected significantly by pretreatment method (Feldman and Beaudoin 1991). Comparing different pretreatment methods, Konecny and Naqvi (1993) suggested that solvent exchange method keeps better the microstructure for MIP and this was later confirmed by Muller and Scrivener (2017) comparing pore size distribution from MIP with the results from ^{1}H-NMR. From theoretical point of view, analysis of MIP results from Eq. (5) is also sensitive to the values of surface tension and contact angle between mercury fronts and pore walls of cementitious materials. The value of surface tension between Mercury and cement paste is generally accepted to be equal to 0.48 N/m (e.g., (Powers et al. 1954; Taylor 1997)). However, different values were reported for contact angle, probably because the contact angle is sensitive to many parameters such as the age of sample, roughness of the surface, pretreatment and the purity of Mercury. Shi and Winslow (1985) measured the contact angle between 123 and 135°, and observed that the contact angle may vary depending on cement composition, age of the cement paste and pretreatment. Adolphs et al. (2002) found the contact angle to be dependent on equilibrium relative humidity and wetting–drying

cycle of the sample before measurement, and reported values between 142 and 150°. The dependency of contact angle on intrusion–extrusion cycle has been studied in Zeng et al. (2012) by defining a hysteresis factor between contact angle of intrusion cycle and extrusion cycle. Recently, a much lower value of 120° was proposed based on the comparison of MIP and ^{1}H-NMR (Muller and Scrivener 2017). By comparison between the volume of capillary pores obtained from MIP and that from ^{1}H-NMR, they also suggested that the so-called ink-bottle effect is minor for the range of pores that can be seen by MIP (Muller and Scrivener 2017), which is not consistent with the point of view in many other articles, such as Diamond (2000). While reviewing MIP technique for cementitious materials, Diamond (2000) argued that the pore size seen in MIP measurement is not the size of pore but the size of pore entry, which is accepted by many others. For instance, Zeng et al. (2019) called the result of MIP as throat size distribution (TSD) and studied the pore size distribution from mercury extrusion data. Seen from Eq. (5), the range of pore size that can be detected by MIP depends on the value of applied pressure. For the maximum pressure applied in common MIP tests, the corresponding minimum pore size that can be detected by MIP is around 4 nm as resumed in Fig. 2. Hence, MIP cannot see internal structure of C–S–H whose size is smaller than this usual range. More suitable method to characterize the C–S–H is sorption isotherms which will be reviewed in detail in Sect. 2.

There are other indirect methods that use water inside the cement paste as probe, such as low-temperature calorimetry (LTC), ^{1}H-NMR, Small-angle scattering (SAS, includes Small-angle X-ray scattering (SAXS) and small-angle neutron scattering (SANS)). Main advantages of these methods are that the samples can be measured 'as prepared', so pore structure is not disturbed before measuring. The principle of LTC is to link the pore size to the heat emitted during cooling of pore water, based on Gibbs–Thomson equation (Beddoe and Setzer 1990; Fagerlund 1973; Tombari et al. 2005). In experiment, temperature of sample is decreased gradually from 20 to -60 °C, while the heat flow is recorded as a function of temperature (Fagerlund 1973). Though the LTC is relatively fast and young samples can be measured, the results are affected by rate of temperature change, alkali concentration in the pore solution (Kjeldsen and Geiker 2008). Furthermore, due to strong adsorption forces, water in interlayer space do not freeze even at -42 °C (Bager and Sellevold 1986; Brun et al. 1977), at which the last peak of heat emission is observed. Maruyama et al. (2018) quantified that only 20% of the total evaporable water was frozen. Hence, it is difficult to observe pore structure in C–S–H by LTC. Cracks can be caused

during ice formation and affect the measurement results. To improve the LTC analysis, Kjeldsen and Geiker (2008) recommended adding nucleation agent and correcting measurement temperature for non-equilibrium between the sample and the reference block. Comparing to LTC, ^{1}H-NMR and SAS are non-destructive techniques. How to analyze pore structure from ^{1}H-NMR and SAXS/SANS will be reviewed in Sects. 3 and 4, respectively.

After reviewing the above-mentioned methods, influence of pretreatment methods on sorption measurement will be compared. Pore size distribution and specific surface area will be analyzed from different experimental methods on white Portland cement paste.

2 Sorption Isotherm

Sorption isotherm is the oldest and most widely used technique to measure the surface area of cement paste, and probably with the most published results (Thomas et al. 1999). In this section, first, we review different methods that have been used in literature to measure sorption isotherms for cement paste. Then, BET sorption theory will be presented for calculation of specific surface area, followed by estimation of pore size distribution by BJH method and the local density method.

2.1 Experimental Methods

Sorption isotherms consist in measuring the amount of condensed liquid of an adsorbate on the surface of an adsorbent, while controlling the relative pressure p/p_{sat} at a constant temperature. Generally, there are gravimetric and volumetric methods to determine the adsorbed amount. In the gravimetric method, samples are put into a chamber with controlled relative humidity. Mass of the sample is weighted until equilibrium is reached between the relative pressure in the chamber and the sample. Then, measurement is moved to the next target relative humidity step by step. In the volumetric methods (also called manometric methods), known amount of adsorbate gas is introduced into sample chamber where the gas pressure is monitored. By adding or removing gas molecules, an equilibrium is achieved at the target relative pressure. Then, amount of adsorption is calculated from ideal gas equation.

Water vapor and nitrogen are the two adsorbates used most widely for the sorption measurement of cement paste. In addition, many other gas have also been used as adsorbate for the sorption measurement of cement paste, for instance, oxygen (Blaine and Valis 1949), argon (Blaine and Valis 1949; Vidick 1987), krypton (Vidick 1987), organic vapors (Mikhail and Selim 1966), ammonia (Odler 2003). Important aspects to consider when choosing an adsorbate are as follows: the heat of adsorption, the size of gas molecules, the polarity of gas
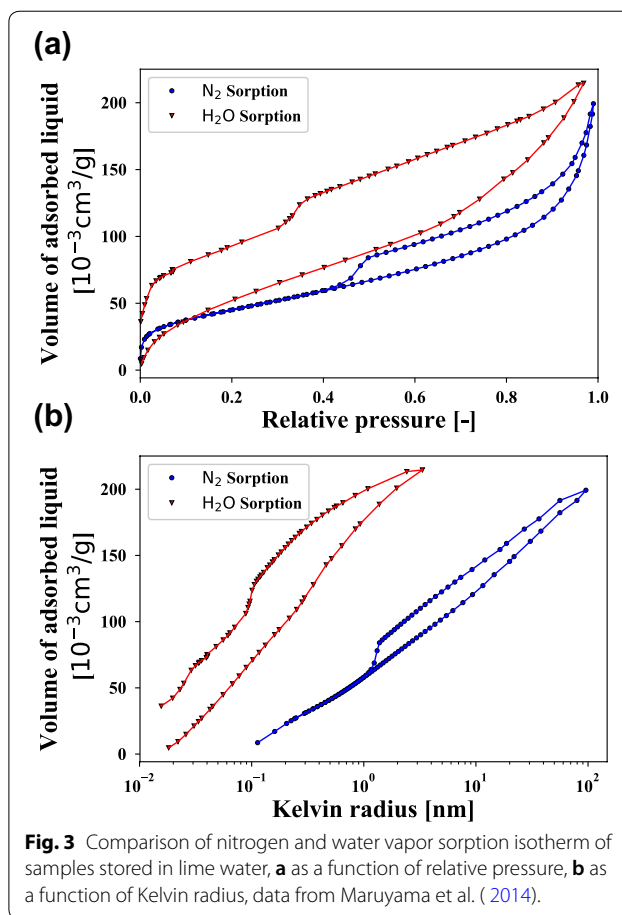

Fig. 3 Comparison of nitrogen and water vapor sorption isotherm of samples stored in lime water, **a** as a function of relative pressure, **b** as a function of Kelvin radius, data from Maruyama et al. (2014).

molecules and chemical reactivity with cement paste (Thomas et al. 1999). In this review, we focus only on water vapor and nitrogen sorption isotherms.

Generally, the adsorption amount, when expressed in volume of liquid, is less in nitrogen sorption comparing to that in water vapor sorption. Said otherwise, sorption capacity and surface area measured by nitrogen sorption are smaller comparing to that measured by water vapor sorption. An example of comparison is shown in Fig. 3a, on white Portland cement paste, with water–cement ratio 0.55 (data from Maruyama et al. (2014)), by the volumetric method. Pretreatment is necessary for the volumetric method since the starting state should be under vacuum in most of the sorption devices. Samples are crushed into powder (sizes of particles are in between 25 μm and 75 μm) prior to the test and dried under vacuum condition at 20 °C. Nitrogen sorption was measured at -196 °C (BELSORP-miniII MicrotracBEL. Corp) on 75 ± 5 mg sample, while water vapor sorption was measured at 20 °C (VSTAR, Quantachrome instrument) on 25 ± 1 mg sample. As expected, at given relative pressure, volume of adsorption in nitrogen sorption is less than water vapor sorption. Even when nitrogen and

water vapor sorption isotherms are compared for same Kelvin radius (defined in Eq. (5)), adsorption in nitrogen is still less than water (see Fig. 3b). Such difference has been compared in many articles (e.g., (Odler 2003; Robens et al. 2004)) and different interpretation exists in the literature. It was suggested that due to larger size of a nitrogen molecule (kinetic diameter of 4.05 Å) compared to a water molecule (kinetic diameter of 3.25 Å), nitrogen sorption cannot access smaller pores, but Feldman and Sereda (1968) argued that this tiny difference in size of molecules cannot explain such big difference of adsorption and suggested that water vapor was structurally incorporated or re-adsorbed into C–S–H interlayer space. It was proposed in Brunauer et al. (1970) that the fact that water molecules possess a distinct dipole, whereas nitrogen molecules do not possess, may play a role. Some others suggested that the difference of adsorption amount between nitrogen and water may come from the fact that nitrogen sorption is usually measured at a temperature much lower than water vapor sorption (Brunauer et al. 1970; Hagymassy et al. 1972; Mikhail et al. 1964). Based on the difference of nitrogen sorption and water vapor sorption Jennings (2000); Tennis and Jennings (2000) suggested the existence of Low-Density (LD) C–S–H, to which nitrogen can access and High-Density (HD) C–S–H, to which nitrogen cannot access. Following their work, though not proved experimentally yet, the most popular view on the difference between nitrogen and water vapor sorption is that nitrogen sorption can access only gel pores; whereas, water vapor can see both gel pores and interlayer space (for instance, Maruyama et al. (2014)).

On the contrary, for gravimetric method, measurement can be performed on block samples, not necessarily starting from dry state. When block samples are used, measurement time can be quite long. For instance, up to years for samples with thickness of 5 mm (Baroghel-Bouny 2007), or up to weeks for samples with thickness of 1 mm samples (Maruyama et al. 2015, 2016). As an example, water vapor sorption isotherms measured by different techniques are compared in Fig. 4. The samples are white Portland cement paste, with water–cement ratio 0.55, stored in lime water for at least half year before starting the test. $3 \times 13 \times 100$ mm^3 bar shape sample was dried in different chambers, where relative humidity was controlled by salt-saturated solution, during 1 year, which is noted as the long-term drying method (Maruyama et al. 2014). In the short-term drying method, sorption was measured on sample of size $3 \times 3 \times 1$ mm^3 using RH–TG (denotes for Relative Humidity–Thermo-Gravimetry). Mixture of water vapor and nitrogen was blown constantly into the cell of RH–TG to keep relative humidity at the target value (Maruyama and Rymeš
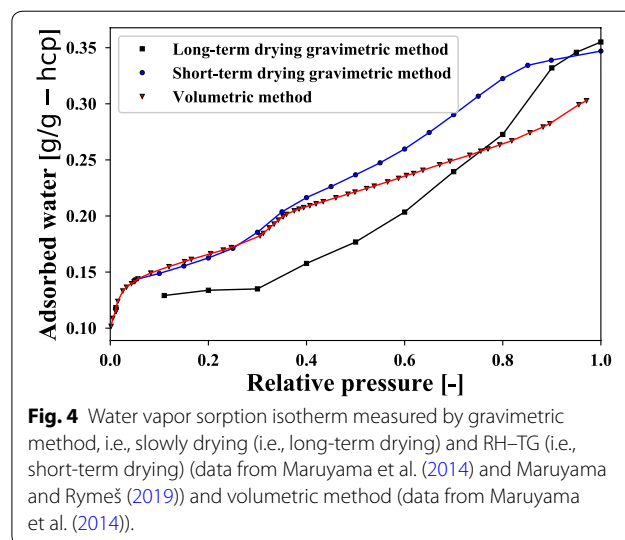

Fig. 4 Water vapor sorption isotherm measured by gravimetric method, i.e., slowly drying (i.e., long-term drying) and RH–TG (i.e., short-term drying) (data from Maruyama et al. (2014) and Maruyama and Rymeš (2019)) and volumetric method (data from Maruyama et al. (2014)).

2019). Each step of relative humidity lasted for 8 h, since more than 90% of mass loss occurred during the first 8 h. To compare with the long-term and short-term gravimetric methods, the desorption branch of the data from Fig. 3 is also plotted as volumetric method in Fig. 4. The sorption amount was normalized with respect to the vacuum-dried mass at 20 °C. We can see from Fig. 4 that the long-term drying method measures more water loss than the short-term drying, which can be explained by the microstructural change of C–S–H due to the long-term drying proposed in Gartner et al. (2017), Maruyama et al. (2014). This difference between short-term and long-term drying method was also acknowledged in Nguyen et al. (2019) and attributed to slowly surface diffusion in nanopores. As for the volumetric method, the sorption amount at higher relative humidity is lower than the short-term drying method, probably due to two reasons: (i) It is difficult in volumetric method to control relative humidity at high values; hence, large pores cannot be fully filled; (ii) More importantly, due to drying of the sample during the pretreatment of volumetric method, some irreversible changes of microstructure happen (Maruyama et al. 2014; Parrott et al. 1980); Influence of different pretreatment method will be compared further in Sect. 5.1.

2.2 Surface Area from Sorption Models
One of the most important information that we get from a sorption isotherm is the surface area of sample. The basic concept of sorption models is to obtain monolayer capacity w_m (i.e., amount of adsorption when sample surface is covered fully by one layer of sorptive molecules) and then calculate surface area by:

$$S = \frac{w_m N_A s}{M_m}, \qquad (1)$$

where M_m and s are the molar mass of adsorbate and cross-sectional area of adsorbate molecule, expressed in [kg/mol] and [m^2], respectively; N_A is the Avogadro's number. The cross-sectional area is measured on the plane of a solid surface, dividing the surface by the number of adsorbed molecules. This cross-sectional area is different from the section calculated from the above-mentioned kinetic diameter. The cross-sectional area of water molecule is equal to 0.114 nm^2 and of nitrogen molecule equal to 0.162 nm^2 (Mikhail and Selim 1966). The monolayer capacity is the key parameter to be obtained by sorption models.

Brunauer, Emmett and Teller (BET) Theory (Brunauer et al. 1938) is the most widely used adsorption model as it can model quite well the sorption isotherm of cement-based material and also thanks to its simplicity. Like many other sorption models, BET model is based on the kinetic approach in which the number of adsorbed and desorbed gas molecules is related to the temperature and the free energy of adsorption. The main hypothesis of BET model is that the adsorption energy is higher in the first layer of adsorption comparing to all the other layers; and for all layers starting from 2nd layer on, the adsorption energy remains the same and equal to that of bulk liquid phase. At equilibrium, summing up the adsorbed molecules of each layer, total adsorption amount is obtained as a function of relative pressure p/p_{sat} as following:

$$\frac{w}{w_m} = \frac{C_{BET} p/p_{sat}}{[(C_{BET} - 1)p/p_{sat} + 1](1 - p/p_{sat})}, \qquad (2)$$

where w is the water content [−]; C_{BET} is the energy constant [−]. For cement pastes, the hypothesis of adsorption of BET theory is generally applicable only in the range of relative humidity 5–35% on the adsorption branch. Hence, the BET Eq. (2) is normally fitted in this range. In practice, the adsorption data are plotted in a linear form,

$$\frac{1}{w(p/p_{sat} - 1)} = \frac{1}{w_m C_{BET}} + \frac{C_{BET} - 1}{w_m C_{BET}} p/p_{sat}, \qquad (3)$$

which is known as the BET plot to obtain the two parameters w_m and C_{BET}. Then inserting the monolayer capacity w_m into Eq. (1), the BET surface S_{BET} area is obtained. As reviewed in Sect. 2.1, water vapor can be adsorbed more than nitrogen, resulting in higher water vapor surface area S_{H_2O} than nitrogen surface area S_{N_2}. It is generally assumed, though not proved yet, that the difference between the water vapor surface area S_{H_2O} and nitrogen surface area S_{N_2} is the surface area of interlayer space of

C–S–H (Maruyama et al. 2014; Maruyama et al. 2017). Although only adsorption branch of sorption isotherms is used to evaluate the BET-specific surface area Maruyama and Igarashi (2011) observed that the desorption branch of water vapor sorption isotherm also follows well the BET theory. This may be due to the fact that, in the desorption branch of sorption experiment, the water adsorbed in the interlayer space of C–S–H layers does not evaporate until very low pressure. The desorption only from gel pores, i.e., outer surface of C–S–H may correspond the hypothesis of the BET theory.

Other sorption models have been also used sometimes. Older than BET model, Langmuir model (Langmuir 1918) assumes only monolayer adsorption and suites well for chemisorption. Guggenheim–Anderson–de Boer (GAB model) extended the applicability of BET theory on whole range of relative humidity (Anderson 1946; Brunauer et al. 1969; Timmermann 2003). Comparing to BET theory, GAB model introduced one more energy constant to differentiate the adsorption energy of second layer from that of all other subsequent layers. In Anderson (1946) the BET theory was generalized by distinguishing the adsorption energy of each layers. The Langmuir theory, BET theory and GAB model can regarded as one of the specific cases of the generalized BET theory (Anderson 1946; Baroghel-Bouny 1994). Recently, Nguyen et al. (2019, 2020) modified the BET theory by taking into account the reduction of the adsorption surface with the increase of number of absorbed layers. Despite these progresses, BET surface area remains for the moment the mostly reported values in literature.
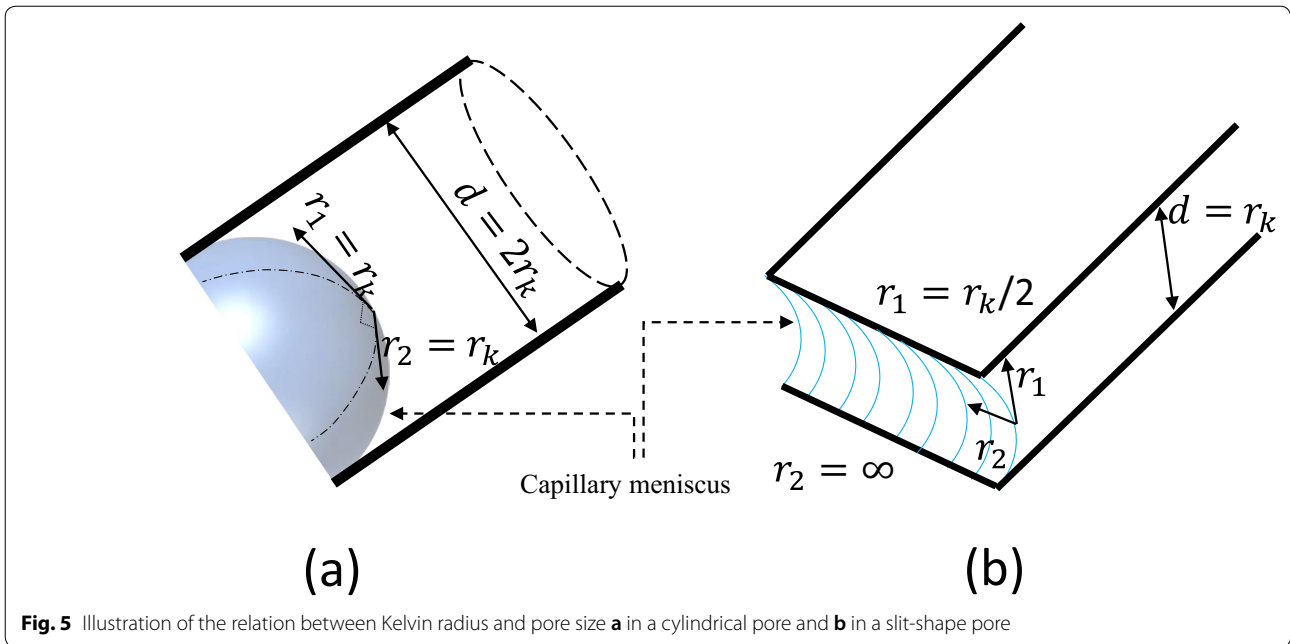
2.3 Pore Size Distribution by BJH Model

Inferring pore size from sorption isotherm is more laborious than inferring the specific surface area. Though various models have been proposed in literature, in this section, we review basics of BJH method, without going into details of numerical techniques.

During a sorption measurement, condensation of gas is governed by Kelvin's law (Coussy 2011), which was obtained by equating the chemical potential μ_L of the condensed liquid phase and μ_G of gas phase of the adsorbate. Kelvin's law relates the capillary pressure P_c, which is the pressure difference between liquid phase and gas phase, to the relative pressure by:

$$P_c = \frac{\rho_l R T}{M_m} \ln(p/p_{sat}), \qquad (4)$$

where ρ_l is the density of liquid phase, expressed in [kg/m^3]. R is the universal gas constant, equal to 8.314 J/mol/K and T is the absolute temperature. Due to this capillary pressure P_c, the interface between condensed liquid

Fig. 5 Illustration of the relation between Kelvin radius and pore size **a** in a cylindrical pore and **b** in a slit-shape pore

and gas is not flat but forms a curved meniscus. Radius of the capillary meniscus is also related to capillary pressure via Laplace equation (e.g., see Sect. 6.1.7 in (Coussy 2011)) or known also as Washburn's equation (Gardner 1921; Muller and Scrivener 2017):

$$r_k = -\frac{2\gamma\cos\theta}{P_c}, \tag{5}$$

where r_k is the mean radius of the capillary meniscus, expressed in [m], θ is the contact angle between adsorbate and solid surface and γ is the surface tension of adsorbate, expressed in [N/m]. For water and nitrogen, the contact angle is considered to be 0. The surface tension depends on temperature. For water, surface tension is equal to 0.072 N/m at 20 °C; for nitrogen, equal to 0.0089 N/m at −196 °C. For a given relative humidity, combining Eqs. (4) and (5), radius r_k of meniscus is obtained and named as Kelvin radius. At each step of sorption measurement, when equilibrium is reached, capillary meniscus only with the corresponding Kelvin radius remains.

The relation between pore size and Kelvin radius depends on the assumption of the pore geometry. Figure 5 illustrates geometrical relation between Kelvin radius r_k and pore diameter d for cylindrical pore and slit pore. In a cylindrical pore, the meniscus has a spherical shape which leads to a pore diameter $d = 2r_k$; whereas in slit shaped pores, the meniscus is cylindrical and the pore width would be $d = r_k$ (Lowell 2005).

The BJH method (Barrett 1951), also called modified Kelvin equation, considers that the condensed liquid

has two parts: one is capillary liquid, whose volume depends on relative pressure via Kelvin–Laplace equation; the other is adsorbed layer on pore surface, whose thickness may be considered as a function of relative pressure. When relative pressure changes, both capillary liquid and adsorbed thickness change. Letting sum of the volume change of capillary and adsorbed liquid equal to the experimentally measured adsorbed amount change, an explicit equation of pore size can be obtained. Solving this equation for whole range of adsorption, a pore size distribution can be obtained. Exact expression of BJH method and an approximated expression were derived in Halenda (1951) for cylindrical pore. It should be kept in mind that, considering the geometrical relation illustrated in Fig. 5, the equation of BJH method is different when different pore shape is assumed. For instance, Brunauer et al. (1967) compared volume, surface area and pore size from BJH model for cylindrical, slit and spherical pores. Hence, to summarize, BJH model includes three inputs: pore shape, Kelvin–Laplace equation and a model to estimate adsorption thickness.

Different models for adsorption thickness have been used in literature (e.g., see chapter 8 in Lowell (2005)). For instance, both Langmuir sorption model and the BET model in Eq. (2) have been used in Pinson et al. (2015) to estimate thickness of adsorption of water sorption isotherm. Adsorption thickness proposed by Hagymassy et al. (1969) was also widely used in pore structure analysis from water vapor sorption isotherm (Zeng et al. 2014). Again for water sorption isotherm, in calculation
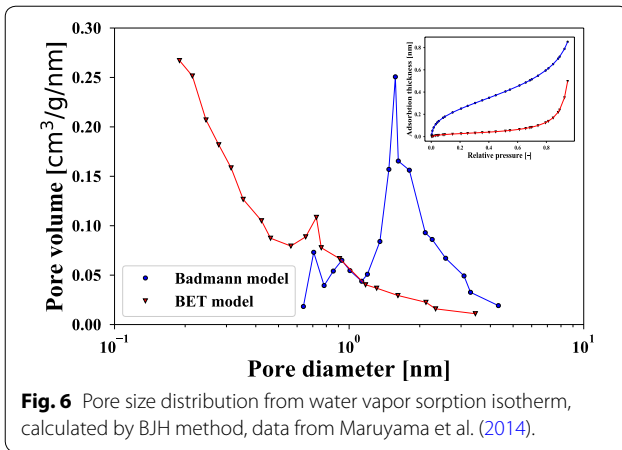
Fig. 6 Pore size distribution from water vapor sorption isotherm, calculated by BJH method, data from Maruyama et al. (2014).

of drying shrinkage, (Maruyama et al. (2017b), Maruyama and Igarashi (2011) used the Badmann model in Eq. (6) proposed by Badmann et al. (1981):

$$t(h_r) = K_1 - K_2 \ln(-\ln(h_r)), \tag{6}$$

where t is the thickness of adsorption in nanometer; parameters K_1 and K_2 are expressed in nanometer. As for nitrogen sorption, Harkins–Jura model (Harkins and Jura 1944),

$$t(h_r) = \left(\frac{13.99}{0.034 - \log_{10} h_r} \right)^{1/2}, \tag{7}$$

expressed in nanometer, is widely used. When different thickness models are used, BJH model may give totally different pore size distributions. Figure 6 displays an example of pore size distribution from adsorption branch of water vapor sorption displayed in Fig. 3. The parameters of Badmann model were fitted on adsorption branch in the range of relative humidity between 3 and 10%. It can be seen from Fig. 6 that BET model and Badmann model gives very different pore size distribution. Hence, it is important to keep in mind that the adsorption thickness model could be crucial for the evaluation of pore size distribution from BJH method.

2.4 Pore Size Distribution by Density Functional Approach

If the BJH method is considered as backward problem, then the corresponding forward problem would be to estimate sorption isotherm from known pore size distribution. Assuming the pore size distribution function as $f(\phi)$,[1] the sorption isotherm reads as:

---

[1] In this particular Sect. 2.4, pore diameter is noted as ϕ to avoid confusion with the differential symbol d.

$$w(h_r) = \int_{\phi_{min}}^{\phi_{max}} f(\phi) \rho_L(\phi, h_r) d\phi, \tag{8}$$

with ϕ_{max} and ϕ_{min} are maximum and minimum pore size, respectively; $\rho_L(\phi, h_r)$ is the quantity of liquid per unit volume of pore with size ϕ under given relative humidity. $\rho_L(\phi, h_r)$ is called the density function, depends on pore size and should not be confused with the density of bulk liquid ρ_l, which is an intrinsic property of the liquid itself. If the density function $\rho_L(\phi, h_r)$ can be estimated for each pore size a priori, then assuming some type of pore size distribution function, by back-fitting Eq. (8) on the measured sorption isotherm, we can obtain the pore size distribution. The main task of this type of density functional approach is to estimate the density function $\rho_L(\phi, h_r)$.

The most common way in literature of cementitious material is to calculate $\rho_L(\phi, h_r)$ as the sum of condensed liquid (capillary part) and adsorbed liquid, same way as BJH (e.g., (De Burgh et al. 2016; Jiang et al. 2019; Wang et al. 2018)). Other more sophisticated ways within the frame of statistical physics were also used in (Lastoskie et al. 1993a, b) on sorption isotherm of carbon.

From thermodynamic point of view, the ensemble of liquid molecules in a pore at a given relative humidity and temperature is a Grand Canonical ensemble. Said otherwise, temperature T, volume V and chemical potential μ of the system are given. Thermodynamic equilibrium state of such a grand canonical ensemble can be simulated by minimizing the grand potential $\Omega(T, V, \mu)$ (a measurement of energy, similar to Gibbs free energy or enthalpy) of the system in molecular dynamics or by Grand Canonical Monte Carlo (GCMC) simulation. Lastoskie et al. (1993a, b) proposed the non-local density functional theory (NLDFT) by considering interaction between liquid–liquid and liquid–solid molecules. They compared the density function $\rho_L(\phi, h_r)$ as well as pore size distribution $f(\phi)$ obtained from NLDFT with those obtained by Kelvin–Laplace equation, BJH model and GCMC. It was acknowledged in Lowell (2005) that NLDFT and GCMC are the most accurate methods for pore size analysis of very narrow pores. As for cementitious materials, Wenzel et al. (2017) estimated pore size distribution of C–S–H from argon sorption isotherm using NLDFT and compared with TEM observation results. GCMC were used to estimate amount of adsorption in virtual 3D microstructure of C–S–H, for noble gases in Pellenq and Levitz (2002) and for water in Ioannidou et al. (2016). However, these methods are not widely used in pore size analysis of cement paste, probably due to the difficulty in identification of interaction forces between C–S–H layers and water molecules.

3 Proton Nuclear Magnetic Resonance Relaxometry

Proton nuclear magnetic resonance relaxometry is a non-destructive technique (Scrivener et al. 2016) to investigate the confined state of water in pores of cement paste. The ^{1}H-NMR was applied on cement paste for the first time in Japan in Kawachi et al. (1955) to study the ratio between chemically bounded water and free water as a function of hydration. Later, the relaxation time was measured to study evaporable water of cement paste in Blinc et al. (1978). Since then, many authors (for instance (Apih et al. 2001; Barbic et al. 1982; Blinc et al. 1988; Halperin et al. 1994; Jehng et al. 1996; McDonald et al. 2005; Schreiner et al. 1985; Valori et al. 2010)) contributed to the progress of the study of evaporable water state in cement paste by relaxation measurement of ^{1}H-NMR. General review of application of ^{1}H-NMR in cement paste can be found in the review papers by Valori et al. (2013). Now, experimental protocol of relaxation measurement and data analysis of ^{1}H-NMR experiment have been established and well documented (see chapter 7 in Scrivener et al. (2016)).

In natural state, the proton (^{1}H) like all other atomic nuclei has a spin–spin rotation moment. The directions of the spin of the proton are randomly distributed in the water inside of the sample. In ^{1}H-NMR, external magnetic pulses are applied to align spin directions inducing magnetic field. Once the external magnetic field is removed, it takes certain time for the spin directions to gradually go back to the original random state, which can be measured by the decay of the signal intensity of the induced magnetic field. From the decay of signal, T_2 relaxation (spin–spin relaxation) time can be calculated. This T_2 relaxation time depends on the confining state of water, from which we can infer information about pore size.

In ^{1}H-NMR experiment, no pretreatment is required and sample can be used as prepared. For cement paste, generally, two series of magnetic fields are applied to measure the relaxation times: Quadrature Echo (QE) sequence (or, called as solid-echo (SE)) for chemically bounded water and CPMG pulse sequence for evaporable water. For the details, readers can refer to chapter 7 in Scrivener et al. (2016). This section focuses on the evaluation pore size and specific surface area from the typical results of ^{1}H-NMR experiment.

In CPMG measurement, the decay of signal intensity of induced magnetic field is deconvoluted and four peaks are observed at different T_2 relaxation times. Figure 7 (top) shows T_2 relaxation time of a matured white Portland cement with water–cement ratio 0.55 (data from Maruyama et al. (2019)). Four peaks observed in Fig. 7 correspond to (from left to right) interlayer water,
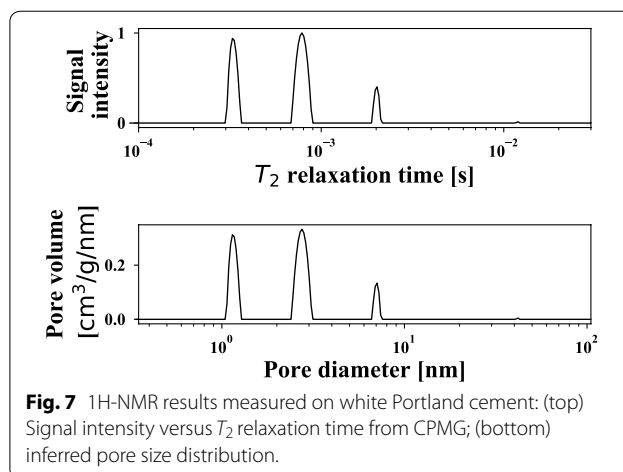

Fig. 7 1H-NMR results measured on white Portland cement: (top) Signal intensity versus T_2 relaxation time from CPMG; (bottom) inferred pore size distribution.

gel water, interhydrate water and capillary water (Muller et al. 2013). Size of the peak corresponds to the amount of water. Knowing the amount of chemically bounded water from QE sequence, volume of water in each type of pores can be computed. Two models are proposed in literature for estimation of the pore size: relaxivity method and amplitude method.

The relaxivity method is known as fast exchange model as it is based on "fast exchange" hypothesis: to relax the spin alignment, a water molecule in the bulk of a pore has to exchange first its position with a water molecule on surface of pore. Supposing that this exchange process is much faster than the relaxation of spin, relaxation rate in a given pore should be proportional to the ratio S/V of surface over volume (D'Orazio et al. 1990). This hypothesis reads as following:

$$\frac{1}{T_2} = \frac{V - \varepsilon S}{V} \frac{1}{T_2^{\text{bulk}}} + \frac{\varepsilon S}{V} \frac{1}{T_2^{\text{surf}}} \approx \frac{S}{V} \frac{\varepsilon}{T_2^{\text{surf}}}, \qquad (9)$$

where T_2^{bulk} and T_2^{surf} are the T_2 relaxation times of bulk water and surface adsorbed water, respectively; ε is the thickness of monolayer adsorbed water, taken to be the height of one water molecule, 0.28 nm. If the pore shape is assumed to be slit, the size (width) of pore can be computed as:

$$d = 2\varepsilon \frac{T_2}{T_2^{\text{surf}}}. \qquad (10)$$

Then, combining the pore size with the volume of corresponding type of water, surface area can be computed.

Key factor for applying the fast exchange model is the value of relaxation time T_2^{surf} of surface adsorbed water, which can be measured by ^{1}H-NMR experiment on material dried to mono-layer coverage. The difficulty lies in the definition of mono-layer covered dried state. In

addition, the measured relaxation time T_2^{surf} depends on cement type, mixture proportion and the device of ^{1}H-NMR. The density of elements that can be easily magnetized has also a large impact on the relaxation time T_2^{surf}. For example, Halperin et al. (1994) measured the surface relaxation time on a sample with water–cement ratio 0.43 which was dried to lower than 20% of saturation degree and obtained 0.04 ms. Bohris et al. (1998) reported a value of 0.01 ms on cement paste with water–cement ratio 0.3 ms and 0.5 ms; whereas, 0.085 ms was measured on mortar sample by (Valckenborg et al. (2001). For white Portland cement with water–cement ratio of 0.4, Muller et al. (2013) measured the relaxation time 0.075 ms. Different values of surface relaxation time were measured in Zhou et al. (2018), on samples that were equilibrated at 33% of relative humidity. To show an example, pore diameters displayed in Fig. 7 (bottom) are computed with Eq. (9) taking relaxation time T_2^{surf} of surface adsorbed water equal to 0.176 ms.

The amplitude model, proposed in McDonald et al. (2010), is based on the amplitude of NMR signals rather than the relaxation time. In this model C–S–H is considered as layered structure. When pores are saturated with water, it is assumed that all water molecules are in fast exchange and only one relaxation time is observed. When the sample is dried, two relaxation times are supposed: one from water on the pore surface, which has lower relaxation time but increasing amplitude with increase of drying; the other from bulk water molecules, which has same relaxation time as saturated state but decreasing amplitude with increase of drying. Therefore, ^{1}H-NMR experiments should be performed at different stages of drying. McDonald et al. (2010) showed that the pore sizes from amplitude model were in a good agreement with the fast exchange model. Given the fact that more assumption and experiments are needed in amplitude model comparing to fast exchange model, only the fast exchange model will be used in discussion section.

4 Small-Angle Scattering

Small-angle X-ray scattering was used to determine specific surface area of cement paste for the first time by (Winslow and Diamond 1974). Since then, both SAXS and SANS were widely applied to characterize complex microstructure of cementitious materials (Allen et al. 2007; Allen and Livingston 1998; Allen and Thomas 2007; Bogner et al. 2020; Maruyama et al. 2017b; Thomas et al. 1998, 1999). An incident beam of either X-ray (in SAXS) or neutron (in SANS) is passed through the material. Due to the interaction between microstructure of the material and the incident beam, small component is scattered out from the direction of the incident beam. The intensity of

X-ray or neutron is measured as a function of scattering angle. In SAXS, X-rays interact with outer shell electrons; whereas, in SANS, the neutrons interacts with atomic nuclei. For porous materials such as cement paste, X-ray probes the solid–pore interface where the scattering contrast is maximum. Measured X-ray scattering pattern $I(q)$ (i.e., intensity pattern) is a form of Fourier transform of the solid–pore interface (Brisard et al. 2019; Thomas et al. 1999). Allen et al. (Allen 1991) concluded that the C–S–H gel is the primary source of the scattering. One of the main advantages of SAXS and SANS is that no pretreatment is required and samples can be measured as prepared. Generally, we have to use block samples but not powder, because surface roughness and particle size will add some scattering signal on the data. The range of microstructure that can be measured by SAXS and SANS is wide, up to 3 orders of magnitude (Maruyama 2017b). However, the main difficulty remains on data analysis and exploration of the results. In the following, methods of surface area calculation are presented only for SAXS.

SAXS results are expressed as the relation between scattering intensity I (expressed usually in m^{-1}) and scattering vector q (expressed in nm^{-1}), which is obtained by $q = 4\pi \sin(\varphi/2)/\lambda$, where φ is half of the scattering angle and λ is the wave length of X-ray. The relation $I(q)$ follows a power-law in a limited range of q for many materials. In Porod regime, i.e., for instance such as 0.1 nm$^{-1} < q < 1$ nm^{-1} (Porod et al. 1982), the scattering intensity is proportional to the volumetric specific surface area S_v (expressed in m^2/m^3). In practice, a linear relationship can be fit between Iq^4 and q^4, to obtain the volumetric specific surface area:

$$Iq^4 = 2\pi |\Delta\rho_e|^2 S_v + Cq^4, \tag{11}$$

where $\Delta\rho_e$ is the scattering length contrast between solid and pore water (expressed in [m^{-2}]), i.e., between C–S–H and water in the case of cement paste. There are two major issues in applying the Eq. (11): the range of Porod regime and the value of scattering length contrast.

The range of Porod regime is affected by the typical size of particles of interest that scatter the X-ray. Originally, it was proposed that the range of for Porod regime is in between 0.1 nm^{-1} and 1 nm^{-1} (Porod et al. 1982). Later, Thomas et al. (1998), by comparing the coefficient of correlation for different range of q on SANS data measured on cement paste, suggested that Porod regime is in between 1.4 nm^{-1} and 2 nm^{-1} for C–S–H.

Regarding the scattering length contrast, its value can be calculated from the density and chemical composition of the particles. Noting that number of electrons in one molecule as n_e, density as ρ, electron density would be $\rho n_e N_A/M_w$ (expressed as number of electron per volume, m^{-3}). Multiplying this electron density by Thomson

radius $r_T = 2.82 \times 10^{-15}$ m, X-ray scattering length reads as $\rho_e = \rho n_e N_A r_T / M_w$ (expressed in m^{-2}). Since the exact chemical composition of C–S–H is not fully defined, calculating the X-ray scattering length causes problems. Moreover, the impact of the scattering length contrast in Eq. (8) is significant. For instance, scattering length of $C_{1.7}SH_{1.5}$ is 12% higher compared to that of $C_{1.7}SH_{2.5}$.

In the above Porod regime method, microstructure is obtained from scattering. The inverse problem, i.e., from microstructure to scattering is less ambiguous and analytical fractal models with specified shape for building blocks of C–S–H were proposed in literature. For instance, supposing spheroid building block, Thomas et al.(Pearson et al. 1983) reproduced appropriately the SANS intensity pattern in the range of q lower than Porod regime. Based on the colloidal model of C–S–H (CM-II) proposed by Jennings et al. (2008), Chiang et al. (2012) assumed disk-shape building blocks with layered structure inside and developed fractal disk model to evaluate globule size in the CM-II model. Knowing the average diameter ϕ_d and thickness t_d of disk from the fractal disk model, surface area of C–S–H building block per volume of amorphous C–S–H gel can be estimated. Neglecting surface area of other crystalline hydrates and unreacted clinkers, and if the volume fraction of amorphous C–S–H gel χ can be estimated from other techniques, the volumetric surface area can be calculated as:

$$S_v = \frac{4t_d + 2\phi_d}{t_d \phi_d} \chi. \qquad (12)$$

It is worth noting that the surface area calculated from Eq. (8) differs from that of Porod regime, due to (1) the range of q is lower meaning that the scattering particle size are larger; (2) only surface of building block is taken into account and, hence, interlayer space is neglected. That is to say, Eq. (8) reflects more the surface area of gel pores; whereas Eq. (11) is more corresponding to the interlayer space.

An example of SAXS intensity profile is displayed in Fig. 8. The experimental data are taken from Maruyama et al. (2017b) where the authors measured SAXS on mature white Portland cement paste with water–cement ratio 0.5, kept under water for 1.5 years. Equation (11) is fitted for 3.5 nm$^{-1} < q < 5$ nm^{-1} which corresponds to size of 0.2 nm − 0.3 nm. The illustrated region for fractal disk model is also taken from Maruyama et al. (2017b).

5 Discussion
This section is dedicated to compare different methods based on various experimental results previously published by the authors (e.g., (Maruyama et al. 2014,
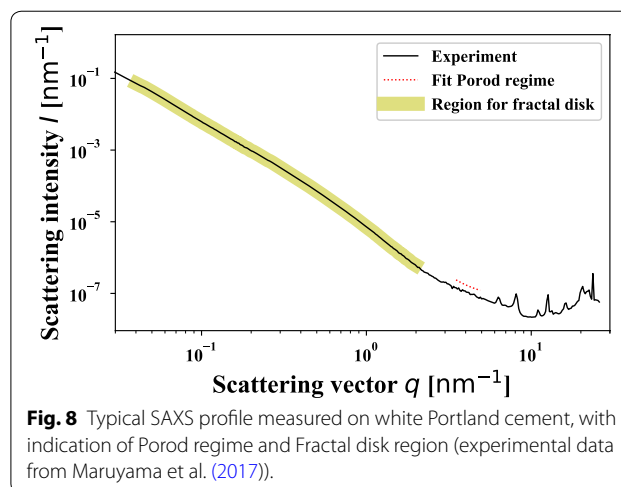
Fig. 8 Typical SAXS profile measured on white Portland cement, with indication of Porod regime and Fractal disk region (experimental data from Maruyama et al. (2017)).

Maruyama et al. 2019; Maruyama et al. 2017b; Sugimoto et al. 2017)). The samples were prepared from white Portland cement, with water–cement ratio 0.55. Except from NMR samples and sorption measurement on 3-day-old samples, all other samples were from the same batch. All samples were stored in lime-saturated water until age of 6 months, and then stored in different relative humidity chambers for at least 1 year before test.

5.1 Comparison of Different Pretreatment on Sorption Isotherm Test
Like MIP, sorption isotherm results are affected by the pretreatment method. Different pretreatment methods had been compared for MIP, for instance, Galle (2001). In Muller and Scrivener (2017), comparing the MIP pore size distribution with ^{1}H-NMR results, solvent exchange was suggested as the best method to keep the original microstructure of the sample. Similarly, Bogner et al. (2020) also concluded that solvent exchange and then drying at 105 °C is the best way to keep the original microstructure of the sample for MIP and nitrogen sorption measurement. However, the influence of pretreatment on the sorption isotherm might be different, since the pores that are seen in the sorption measurement are much smaller than those seen by MIP.

In Sugimoto et al. (2017), different pretreatment methods were applied on both nitrogen sorption isotherm and water vapor sorption isotherm: drying under vacuum at 20 °C during 3 h or at 105 °C during 30 min; solvent exchange with isopropanol or acetone, and then vacuum dry at 20 °C during 3 h or at 105 °C during 30 min. Freeze drying for one week was applied also on nitrogen sorption samples. In each method, the vacuum drying time, either at 20 °C or at 105 °C, should depend on the sample amount. For instance, in this series of test (Sugimoto
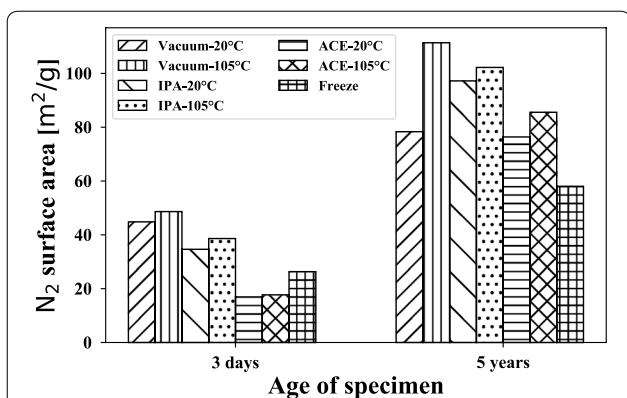
Fig. 9 Influence of pretreatment on nitrogen sorption isotherm, experimental data from Sugimoto et al. (2017).
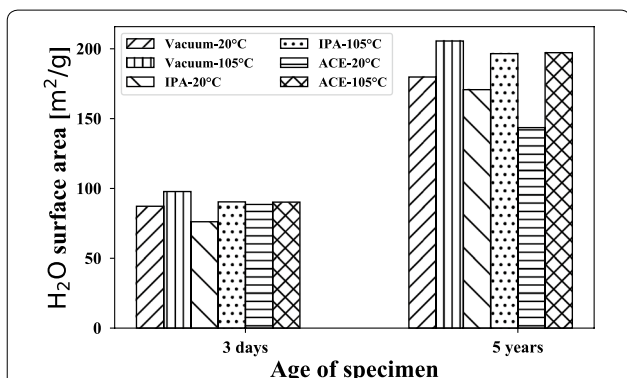

Fig. 10 Influence of pretreatment on water vapor sorption isotherm, experimental data from Sugimoto et al. (2017).

Fig. 11 Comparison of pore size distribution from different techniques. Sorption isotherm data from Maruyama et al. (2014), NMR data from Maruyama et al. (2019). The volume of pores obtained from nitrogen sorption should be read from left Y-axis, while pore volume from water vapor sorption and NMR should be read from right Y-axis.

et al. 2017), drying time that kept best the original microstructure of the sample was found to be 1 h for 25 ± 1 mg of sample, 3 h for 75 ± 5 mg of sample. Considering microstructural change with age of specimen, sorption isotherms were measured on both early age (3-day-old) and mature (5-year-old) cement pastes. Using Eq. (3), BET surface area was calculated. The results are compared in Fig. 9 for nitrogen sorption and in Fig. 10 for water vapor sorption.

From Figs. 9 and 10, it can be seen that vacuum drying at 105 °C provided the highest surface are for both nitrogen and water vapor BET surface area. However, it is known that ettringite and monocarbonate lose water when dried at temperatures even lower than 100 °C (see chapter 5.3 in (Scrivener et al. 2016)). Vacuum drying at 105 °C may reduce number of bounded water molecules per mole of ettringite from 32 to approximately 10–13 (Zhou and Glasser 2001). Rymeš and Maruyama (2018) compared water vapor sorption isotherm on vacuumdried sample at 20 °C and 105 °C. They showed that the total sorption amount and desorption branch of sorption
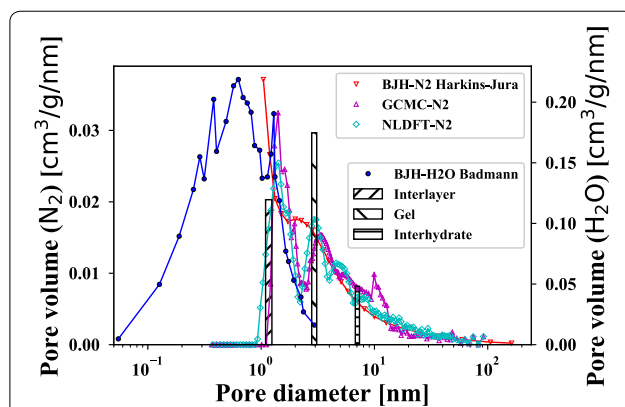
isotherm changed due to decomposition of ettringite. Therefore, stability of hydrates should also be taken into consideration when comparing vacuum drying at 20 °C and 105 °C.

As for solvent exchange method, another drawback is that these solvents are strongly adsorbed on cement paste (Beaudoin et al. 1998; Thomas 1989) and could cause some change in phase composition of cement paste. For instance, it was observed by thermogravimetric (TG) analysis that isopropanol has reacted with portlandite (Beaudoin et al. 1998, 2000; Mikhail and Selim 1966; Zhang and Scherer 2011) As for acetone, similar conclusion was achieved also by TG in Beaudoin et al. (1998, 2000), Taylor and Turner (1987), Zhang and Scherer (2011).

5.2 Comparison of Pore Size Distribution from Different Methods

Nitrogen sorption and water vapor sorption see different parts of the pore structure. As seen in Sect. 2.3, different theories can be applied to analyze pore size form a given sorption isotherm. Besides, the interpretation of the pore size from sorption isotherm and NMR is based on different hypothesis. This section aims at comparing pore size from different experiments and different analysis methods.

In Fig. 11, pore size distributions of mature white Portland cement pastes from various methods are compared. All samples are stored in lime-saturated water before test. From nitrogen sorption data (see Fig. 3), we calculated the pore size distribution using three different methods, all with slit pore assumption: (1) BJH model, with Harkins–Jura model (Eq. (7)) as adsorption thickness model;

(2) GCMC simulation, (3) NLDFT, both using BELMaster7 software (MicrotracBEL. Corp) and properties of carbon for solid–liquid interaction parameters. Pore size distribution is also computed from water vapor sorption isotherm (see Fig. 3) using BJH model with slit pore shape and BET model (Eq. (2)) as the adsorption thickness model. These results are compared with NMR pore size distribution, calculated from fast exchange model (Eq. (10), surface relaxation time taken as 0.176 ms).

It can be seen from Fig. 11 that pore size distributions obtained from the same experimental results (here, nitrogen sorption isotherm) could be different. BJH method suggests no peaks in its range; while, both GCMC and NLDFT simulation suggest three peaks. The three peaks of GCMC are at around 1.2 nm, 3 nm and 10 nm, respectively; whereas those of NLDFT are at around 1.2 nm, 3 nm and 5 nm, respectively. The range of pore size obtained from water vapor sorption is smaller comparing to those from nitrogen sorption and NMR, which might be due to the difficulty in establishing adsorption thickness model adequately. In spite of the difference, pore size distributions from different methods show some consistency in Fig. 11. The pore size 7 nm of interhydrate water from NMR is in between the largest size from GCMC and that from NLDFT. The pore size of 3 nm of gel water from NMR corresponds well to the middle peak of both GCMC and NLDFT. In addition, the size of interlayer space from NMR corresponds approximately to the smallest peak position from GCMC and NLDFT of nitrogen sorption isotherm, as well as the first peak of the water vapor sorption isotherm. However, this consistency of interlayer size should be interpreted carefully, since it was believed that nitrogen molecules cannot enter interlayer space and therefore, information about interlayer space size cannot not be obtained from the nitrogen sorption isotherm. As a conclusion, the calculated pore size distribution of cement paste is affected not only by the experimental technique itself but also by the interpretation method of experimental results. Combining multiple techniques would be useful to get a more comprehensive understanding of the pore structure.

5.3 Comparison of Surface Area from Different Methods

Similar to pore size distribution, surface areas measured by different techniques differ from each other, depending on the experimental technique and analysis method. Objective of this section is to compare surface area obtained from different methods. Maruyama et al. (2014) concluded that the microstructure of C–S–H alternates due to the long-term slowly drying. Since the surface area of cement paste originates mainly from C–S–H, the equilibrium relative humidity of the sample (i.e., relative
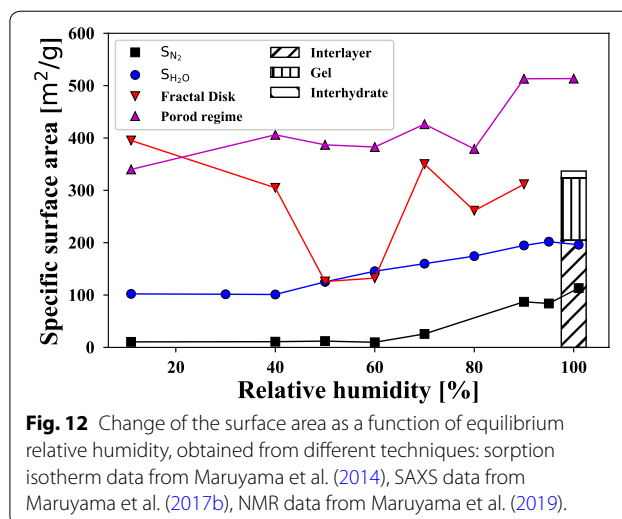

Fig. 12 Change of the surface area as a function of equilibrium relative humidity, obtained from different techniques: sorption isotherm data from Maruyama et al. (2014), SAXS data from Maruyama et al. (2017b), NMR data from Maruyama et al. (2019).

humidity of the storage chamber) is chosen as a comparison index for the surface area.

Figure 12 displays the surface area of white Portland cement paste with water–cement ratio 0.55, obtained from different techniques. Nitrogen surface area S_{N_2} and water vapor surface area S_{H_2O} are computed using BET theory from the experimental results in Fig. 3. With the experimental protocol and used devices of the laboratory, the relative error of nitrogen surface area S_{N_2} and water vapor surface area S_{H_2O} were around $\pm 2.5\%$. Combining the simulation results of SAXS-Fractal Disk model of Maruyama et al. (2017b) and volumetric composition of cement paste obtained from XRD–Rietveld analysis, inserting them into Eq. (12), surface area per volume is calculated. To convert this surface area per volume to surface area per mass of dried hardened cement paste, dry density of cement paste is assumed to be equal to 2.1 g/cm^3 for all equilibrium relative humidity. It is worth noting that the scattering profile variation was within 3% and that the errors related to fitting of disk diameter and thickness, given in Fig. 6 of Maruyama et al. (2017b), were less than 3%. Also using the SAXS data of Maruyam et al. (2017b), we calculated surface area per volume with Porod law Eq. (11). The range of scattering vector is chosen to be in between 3 nm^{-1} and 5 nm^{-1} to correspond the size of C–S–H layers. Scattering length contrast is computed from chemical composition of C–S–H supposing that number of water molecules (number of H in C–S–H) as a linear function of relative humidity, reducing from 4 in saturated state to 1.5 in 11% of equilibrium relative humidity. As for ^{1}H-NMR, surface area is calculated for each type of pores based on the fast exchange model with slit shape of pores. Only saturated sample is analyzed, since when sample is dried, ^{1}H-NMR cannot

see those dried pores. With the repetition number of solid-echo and CPMG signal measurement in the test, the cumulated error of ^{1}H-NMR surface area related to quadrature echo and CPMG measurement and that to relaxation time T_2 obtained by deconvolution algorithm ILT (Inverse Laplace Transform) was around $\pm 5\%$.

It can be seen from Fig. 12 that the surface areas from different method differ from each other significantly. As expected, nitrogen surface area is lower than water vapor surface area, probably due to the fact that nitrogen molecules cannot enter interlayer space. The surface area obtained from SAXS, both fractal disk model and Porod regime, are significantly higher, which is consistent with conclusion in Thomas et al. (1999). ^{1}H-NMR data show surface area higher than sorption data. For the sample stored in lime water, surface area of interlayer space (204 m²/g) alone from ^{1}H-NMR is almost equal the water vapor surface area (196 m²/g), while surface area of gel pore (118 m²/g) is similar to nitrogen surface area (113 m²/g). If we assume that the difference of batch is neglectable, the fact that interlayer surface area (204 m²/g) from ^{1}H-NMR is much higher than the difference between water vapor sorption isotherm and nitrogen sorption isotherm ((196–113=83 m²/g)) suggests that interlayer space may not be the only difference of water vapor sorption and nitrogen sorption isotherms. Though there is discrepancy between surface area measured by different techniques, all of them are able to detect the decrease of surface area due to the microstructural change of C–S–H structure during long-term drying. Hence, it would be useful to combine various methods to characterize microstructure of cement paste.

6 Conclusion

This article reviewed three experimental methods that are used for analysis of pore size distribution and specific surface area of cement based materials: sorption isotherm, proton nuclear magnetic resonance relaxometry and small-angle scattering. Different pretreatment methods are compared for sorption isotherm, for both early age and mature cement paste. We also compared pore size distribution and specific surface area of the same cement paste, using data of different experimental method from literature and analyzed difference and consistency between different methods. Following conclusions are drawn:

- For both early age and mature cement paste, drying under vacuum at 105 °C gives the highest specific surface area in nitrogen sorption and water vapor sorption. However, decomposition of ettringite when dried at 105 °C should be paid attention since the sorption capacity is affected.
- Pore size distribution computed using BJH model from sorption isotherm is sensitive to adsorption thickness model.
- Pore size distribution computed using GCMC or NLDFT from nitrogen sorption isotherm showed similar peak position as the pore size of gel and interhydrate computed from ^{1}H-NMR.
- Values of specific surface area from sorption isotherm, ^{1}H-NMR and SAXS differ from each other significantly. However, all of these methods detected reduction of specific surface area due to alternation of C–S–H microstructure under long-term drying.
- To be able to compare and/or combine the reviewed experimental techniques in view of characterization of microstructure of cement pastes, our findings suggest that experiments be performed on samples from same casting and curing condition, at the same age with least possible disturbance on the original microstructure. It would be helpful to design full set of testing campaign for various parameters that cause microstructural changes, such as age, temperature, drying, etc.

Authors' contributions
AA and IM conceived outline of the review. AA carried out the literature review, collected and analyzed data, wrote the manuscript. IM supervised the analysis, reviewed and edited the manuscript. All authors read and approved the final manuscript.

Authors' information
Abudushalamu Aili: Project Assistant Professor, Graduate school of environmental engineering, Nagoya University, Furocho, Chikusa-ku, Nagoya, Aichi, 461-8603, Japan; Email: aili.abudushalamu@d.mbox.nagoya-u.ac.jp.

Ippei Maruyama: Professor, Graduate school of environmental engineering, Nagoya University, Furocho, Chikusa-ku, Nagoya, Aichi, 4618603, Japan; Graduate school of engineering, the University of Tokyo, Hongo, Bunkyo, Tokyo, 113-8656, Japan; Email: i.maruyama@nagoya-u.jp.

Availability of data and materials
The datasets used during the current study are available from the corresponding author on reasonable request.

Competing interests
The authors declare that they have no competing interests.

Author details
[1] Graduate School of Environmental Engineering, Nagoya University, Furocho, Chikusa-ku, Nagoya 461-8603, Aichi, Japan. [2] Graduate School of Engineering, The University of Tokyo, Hongo, Bunkyo, Tokyo 113-8656, Japan.

References

Adolphs, J., Setzer, M. J., & Heine, P. (2002). Changes in pore structure and mercury contact angle of hardened cement paste depending on relative humidity. *Materials and Structures/Materiaux et Constructions, 35*(October), 477–486. https://doi.org/10.1007/BF02483135.

Allen, A. J. (1991). Time-resolved phenomena in cements, clays and porous rocks. *Journal of Applied Crystallography, 24*(pt 5), 624–634. https://doi.org/10.1107/S0021889890012237.

Allen, A. J., & Livingston, R. A. (1998). Relationship between differences in silica fume additives and fine-scale microstructural evolution in cement based materials. *Advanced Cement Based Materials, 8*(3–4), 118–131. https://doi.org/10.1016/S1065-7355(98)00015-7.

Allen, A. J., & Thomas, J. J. (2007). Analysis of C–S–H gel and cement paste by small-angle neutron scattering. *Cement and Concrete Research, 37*(3), 319–324. https://doi.org/10.1016/j.cemconres.2006.09.002.

Allen, A. J., Thomas, J. J., & Jennings, H. M. (2007). Composition and density of nanoscale calcium-silicate-hydrate in cement. *Nature Materials, 6*(4), 311–316. https://doi.org/10.1038/nmat1871.

Anderson, R. B. (1946). Modifications of the Brunauer, Emmett and Teller Equation. *Journal of the American Chemical Society, 68*(4), 686–691. https://doi.org/10.1021/ja01208a049.

Apih, T., Lahajnar, G., Sepe, A., Blinc, R., Milia, F., Cvelbar, R., et al. (2001). Proton spin-lattice relaxation study of the hydration of self-stressed expansive cement. *Cement and Concrete Research, 31*(2), 263–269. https://doi.org/10.1016/S0008-8846(00)00460-9.

Badmann, R., Stockhausen, N., & Setzer, M. J. (1981). The statistical thickness and the chemical potential of adsorbed water films. *Journal of Colloid and Interface Science, 82*(2), 534–542. https://doi.org/10.1016/0021-9797(81)90395-7.

Bager, D. H., & Sellevold, E. J. (1986). Ice formation in hardened cement paste, Part I—room temperature cured pastes with variable moisture contents. *Cement and Concrete Research, 16*(5), 709–720. https://doi.org/10.1016/0008-8846(86)90045-1.

Barbic, L., Kocuvan, I., Blinc, R., Lahajnar, G., Merljak, P., & Zupancic, I. (1982). The determination of surface development in cement pastes by nuclear magnetic resonance. *Journal of the American Ceramic Society, 65*(1), 25–31. https://doi.org/10.1111/j.1151-2916.1982.tb09917.x.

Baroghel-Bouny, V. (1994). *Caractérisation microstructurale et hydrique des pâtes de ciment et des bétons ordinaires et à très hautes performances*. Ecole Nationale des Ponts et Chaussées.

Baroghel-Bouny, V. (2007). Water vapour sorption experiments on hardened cementitious materials: Part I: Essential tool for analysis of hygral behaviour and its relation to pore structure. *Cement and Concrete Research, 37*(3), 414–437.

Barrett, E. P., Joyner, L. G., & Halenda, P. P. (1951). The determination of pore volume and area distributions in porous substances. I. Computations from nitrogen isotherms. *Journal of the American Chemical society, 73*(1948), 373–380. https://doi.org/10.1021/ja01145a126.

Bazant, Z. P. (1972). Thermodynamics of hindered adsorption and its implications for hardened cement paste and concrete. *Cement and Concrete Research, 2*(1), 1–16.

Beaudoin, J. J., Gu, P., Marchand, J., Tamtsia, B., Myers, R. E., & Liu, Z. (1998). Solvent replacement studies of hydrated portland cement systems: the role of calcium hydroxide. *Advanced Cement Based Materials, 8*(2), 56–65. https://doi.org/10.1016/S1065-7355(98)00008-X.

Beaudoin, J. J., Tamtsia, B., Marchand, J., & Myers, H. R. (2000). Solvent exchange in partially saturated and saturated microporous systems length change anomalies. *Cement and Concrete Research, 30*(3), 359–370. https://doi.org/10.1016/S0008-8846(99)00260-4.

Beddoe, R. E., & Setzer, M. J. (1990). Phase transformations of water in hardened cement paste a low-temperature DSC investigation. *Cement and Concrete Research, 20*(2), 236–242. https://doi.org/10.1016/0008-8846(90)90076-A.

Blaine, R. L., & Valis, H. J. (1949). Surface available to nitrogen in hydrated portland cements. *Journal of Research of the National Bureau of Standards, 42*(3), 257–267. https://doi.org/10.6028/jres.042.022.

Blinc, R., Burgar, M., Lahajnar, G., Rožmarin, M., Rutar, V., Kocuvan, I., et al. (1978). NMR relaxation study of adsorbed water in cement and C3S pastes. *Journal of the American Ceramic Society, 61*(1–2), 35–37.

Blinc, R., Lahajnar, G., Umer, S., & Pintar, M. M. (1988). NMR study of the time evolution of the fractal geometry of cement gels. *Physical Review B, 38*(4), 2873–2875. https://doi.org/10.1103/PhysRevB.38.2873.

Bogner, A., Schatz, J., Dehn, F., & Müller, H. S. (2020). Influence of drying on the microstructure of hardened cement paste: A mercury intrusion porosimetry, nitrogen sorption and SAXS Study. *Journal of Advanced Concrete Technology, 18*(March), 83–94. https://doi.org/10.3151/jact.18.83.

Bohris, A. J., Goerke, U., McDonald, P. J., Mulheron, M., Newling, B., & Le Page, B. (1998). A broad line NMR and MRI study of water and water transport in portland cement pastes. *Magnetic Resonance Imaging, 16*(5–6), 455–461. https://doi.org/10.1016/S0730-725X(98)00072-1.

Bossa, N., Chaurand, P., Vicente, J., Borschneck, D., Levard, C., Aguerre-Chariol, O., et al. (2015). Micro- and nano-X-ray computed-tomography: A step forward in the characterization of the pore network of a leached cement paste. *Cement and Concrete Research, 67*, 138–147. https://doi.org/10.1016/J.CEMCONRES.2014.08.007.

Brisard, S., Davy, C. A., Michot, L., Troadec, D., & Levitz, P. (2019). Mesoscale pore structure of a high-performance concrete by coupling focused ion beam/scanning electron microscopy and small angle X-ray scattering. *Journal of the American Ceramic Society, 102*(5), 2905–2923. https://doi.org/10.1111/jace.16059.

Brun, M., Lallemand, A., Quinson, J. F., & Eyraud, C. (1977). A new method for the simultaneous determination of the size and shape of pores: the thermoporometry. *Thermochimica Acta, 21*(1), 59–88. https://doi.org/10.1061/(ASCE)0733-9372(1988)114:3(639).

Brunauer, S., Emmett, P. H., & Teller, E. (1938). Adsorption of gases in multimolecular layers. *Journal of the American Chemical Society, 60*(2), 309–319. https://doi.org/10.1021/ja01269a023.

Brunauer, S., Mikhail, R. S., & Bodor, E. E. (1967). Some remarks about capillary condensation and pore structure analysis. *Journal of Colloid and Interface Science, 25*(3), 353–358. https://doi.org/10.1016/0021-9797(67)90041-0.

Brunauer, S., Odler, I., & Yudenfreund, M. (1970). The new model of hardened Portland cement paste. *Highway Research Record, 326*, 89–101.

Brunauer, S., Skalny, J., & Bodor, E. E. (1969). Adsorption on nonporous solids. *Journal of Colloid and Interface Science, 30*(4), 546–552. https://doi.org/10.1016/0021-9797(69)90423-8.

Chiang, W. S., Fratini, E., Baglioni, P., Liu, D., & Chen, S. H. (2012). Microstructure determination of calcium-silicate-hydrate globules by small-angle neutron scattering. *Journal of Physical Chemistry C, 116*(8), 5055–5061. https://doi.org/10.1021/jp300745g.

Coussy, O. (2011). *Mechanics and physics of porous solids*. Hoboken: Wiley.

D'Orazio, F., Bhattacharja, S., Halperin, W. P., Eguchi, K., & Mizusaki, T. (1990). Molecular diffusion and nuclear-magnetic-resonance relaxation of water in unsaturated porous silica glass. *Physical Review B, 42*(16), 9810–9818. https://doi.org/10.1103/PhysRevB.42.9810.

De Burgh, J. M., Foster, S. J., & Valipour, H. R. (2016). Prediction of water vapour sorption isotherms and microstructure of hardened Portland cement pastes. *Cement and Concrete Research, 81*, 134–150. https://doi.org/10.1016/j.cemconres.2015.11.009.

Diamond, S. (2000). Mercury porosimetry. An inappropriate method for the measurement of pore size distributions in cement-based materials. *Cement and Concrete Research, 30*(10), 1517–1525. https://doi.org/10.1016/S0008-8846(00)00370-7.

Edel'man, D. S., & Sominskii, N. V. K. (1961). Pore size distribution in cement rocks. *Colloid Journal, 23*, 192–196.

Fagerlund, G. (1973). Determination of pore-size distribution from freezing-point depression. *Matériaux et Constructions, 6*(3), 215–225. https://doi.org/10.1007/BF02479036.

Feldman, R. F., & Beaudoin, J. J. (1991). Pretreatment of hardened hydrated cement pastes for mercury intrusion measurements. *Cement and Concrete Research, 21*(2–3), 297–308. https://doi.org/10.1016/0008-8846(91)90011-6.

Feldman, R. F., & Sereda, P. J. (1964). Sorption of water on compacts of bottle-hydrated cement. II. Thermodynamic considerations and theory of volume change. *Journal of Applied Chemistry, 14*(2), 93–104. https://doi.org/10.1002/jctb.5010140207.

Feldman, R. F., & Sereda, P. J. (1968). A model for hydrated Portland cement paste as deduced from sorption-length change and mechanical properties. *Materials and Structures, 1*(6), 509–520.

Feldman, R. F., & Sereda, P. J. (1970). A new model for hydrated portland cement and its practical implications. *Engineering Journal, 53*(8/9), 53–59.

Galle, C. (2001). Effect of drying on cement-based materials pore structure as identified by mercury intrusion porosimetry A comparative study between oven-, vacuum-, and freeze-drying. *Cement and Concrete Research, 31*(10), 1467–1477.

Gardner, W. (1921). Note on the dynamics of capillary flow. *Physical Review, 18*(3), 206–209. https://doi.org/10.1103/PhysRev.18.206.

Gartner, E., Maruyama, I., & Chen, J. (2017). A new model for the C-S-H phase formed during the hydration of Portland cements. *Cement and Concrete Research, 97,* 95–106. https://doi.org/10.1016/j.cemconres.2017.03.001.

Geng, G., Myers, R. J., Li, J., Maboudian, R., Carraro, C., Shapiro, D. A., et al. (2017). Aluminum-induced dreierketten chain cross-links increase the mechanical properties of nanocrystalline calcium aluminosilicate hydrate. *Scientific Reports, 7*(January), 1–10. https://doi.org/10.1038/srep44032.

Hagymassy, J., Brunauer, S., & Mikhail, R. S. (1969). Pore structure analysis by water vapor adsorption: I t-Curves for water vapor. *Journal of Colloid and Interface Science, 29*(3), 485–491. https://doi.org/10.1016/0021-9797(69)90132-5.

Hagymassy, J., Odler, I., Yudenfreund, M., Skalny, J., & Brunauer, S. (1972). Pore structure analysis by water vapor adsorption. III. Analysis of hydrated calcium silicates and portland cements. *Journal of Colloid and Interface Science, 38*(1), 20–34. https://doi.org/10.1016/0021-9797(72)90215-9.

Halperin, W. P., Jehng, J.-Y., & Song, Y. Q. (1994). Application of spin-spin relaxation to measurement of surface area and pore size distributions in a hydrating cement paste. *Magnetic Resonance Imaging, 12*(2), 169–173. https://doi.org/10.1016/0730-725X(94)91509-1.

Hansen, W. (1987). Drying shrinkage mechanisms in Portland cement paste. *Journal of the American Ceramic Society, 70*(5), 323–328. https://doi.org/10.1111/j.1151-2916.1987.tb05002.x.

Harkins, W. D., & Jura, G. A. (1944). A water adsorption method for determination of the area of solid without the assumption of a molecules area and the air as occupied by nitrogen and their molecules on the surface of solid. *Journal of the American Chemical Society, 66,* 1366–1373.

Holzer, L., Indutnyi, F., Gasser, P., Münch, B., & Wegmann, M. (2004). Three-dimensional analysis of porous BaTiO3 ceramics using FIB nanotomography. *Journal of Microscopy, 216*(1), 84–95. https://doi.org/10.1111/j.0022-2720.2004.01397.x.

Ioannidou, K., Krakowiak, K. J., Bauchy, M., Hoover, C. G., Masoero, E., Yip, S., et al. (2016). Mesoscale texture of cement hydrates. *Proceedings of the National academy of Sciences of the United States of America, 113*(8), 2029–2034. https://doi.org/10.1073/pnas.1520487113.

Jehng, Y., Sprague, D. T., & Halperin, W. P. (1996). Pore structure of hydrating cement paste by magnetic resonance relaxation analysis and freezing. *Magazine of Concrete Research, 14*(7), 785–791.

Jennings, H. M. (2000). A model for the microstructure of calcium silicate hydrate in cement paste. *Cement and Concrete Research, 30*(1), 101–116. https://doi.org/10.1016/S0008-8846(99)00209-4.

Jennings, H. M. (2008). Refinements to colloid model of C-S-H in cement: CM-II. *Cement and Concrete Research, 38*(3), 275–289. https://doi.org/10.1016/j.cemconres.2007.10.006.

Jiang, Z., Xi, Y., Gu, X., Huang, Q., & Zhang, W. (2019). Modelling of water vapour sorption hysteresis of cement-based materials based on pore size distribution. *Cement and Concrete Research, 115*(2018), 8–19. https://doi.org/10.1016/j.cemconres.2018.09.015.

Kawachi, K., Murakami, M., & Hirahara, E. (1955). Studies on the hydration and hardening of cement (experimental studies on nuclear magnetic resonance of water molecules in cement). *Bulletin of the Faculty of Engineering, Hiroshima University, 4,* 95–101.

Kjeldsen, A. M., & Geiker, M. R. (2008). On the interpretation of low temperature calorimetry data. *Materials and Structures/Materiaux et Constructions, 41*(1), 213–224. https://doi.org/10.1617/s11527-007-9239-8.

Konecny, L., & Naqvi, S. J. (1993). The effect of different drying techniques on the pore size distribution of blended cement mortars. *Cement and Concrete Research, 23*(5), 1223–1228. https://doi.org/10.1016/0008-8846(93)90183-A.

Lange, D. A., Jennings, H. M., & Shah, S. P. (1994). Image analysis techniques for characterization of pore structure of cement-based materials. *Cement and Concrete Research, 24*(5), 841–853. https://doi.org/10.1016/0008-8846(94)90004-3.

Langmuir, I. (1918). The adsorption of gases on plane surfaces of glass, mica and platinum. *Journal of the American Chemical Society, 40*(9), 1361–1403. https://doi.org/10.1021/ja02242a004.

Lanzón, M., Cnudde, V., De Kock, T., & Dewanckele, J. (2012). X-ray microtomography (μ-CT) to evaluate microstructure of mortars containing low density additions. *Cement & Concrete Composites, 34*(9), 993–1000. https://doi.org/10.1016/j.cemconcomp.2012.06.011.

Lastoskie, C., Gubbins, K. E., & Quirke, N. (1993a). Pore size distribution analysis of microporous carbons: A density functional theory approach. *Journal of Physical Chemistry, 97*(18), 4786–4796. https://doi.org/10.1021/j100120a035.

Lastoskie, C., Gubbins, K. E., & Quirke, N. (1993b). Pore size heterogeneity and the carbon slit pore: A density functional theory model. *Langmuir, 9*(10), 2693–2702. https://doi.org/10.1021/la00034a032.

Lowell, S. (2005). Characterization of porous solids and powders: Surface area. *Pore Size and Density*. https://doi.org/10.1021/ja041016i.

Maruyama, I., Beppu, K., Kurihara, R., & Furuta, A. (2016). Action mechanisms of shrinkage reducing admixture in hardened cement paste. *Journal of Advanced Concrete Technology, 14*(6), 311–323. https://doi.org/10.3151/jact.14.311.

Maruyama, I., Gartner, E., Beppu, K., & Kurihara, R. (2018). Role of alcohol-ethylene oxide polymers on the reduction of shrinkage of cement paste. *Cement and Concrete Research, 111*(May), 157–168. https://doi.org/10.1016/j.cemconres.2018.05.017.

Maruyama, I., & Igarashi, G. (2011). Water vapor adsorption isotherm model of portland cement paste. *Journal of structural and construction engineering, 76*(664), 1033–1041.

Maruyama, I., Igarashi, G., & Nishioka, Y. (2015). Bimodal behavior of C-S-H interpreted from short-term length change and water vapor sorption isotherms of hardened cement paste. *Cement and Concrete Research, 73,* 158–168. https://doi.org/10.1016/j.cemconres.2015.03.010.

Maruyama, I., Kontani, O., Takizawa, M., Sawada, S., Ishikawao, S., Yasukouchi, J., et al. (2017a). Development of soundness assessment procedure for concrete members affected by neutron and gamma-ray irradiation. *Journal of Advanced Concrete Technology, 15*(9), 440–523. https://doi.org/10.3151/jact.15.440.

Maruyama, I., Nishioka, Y., Igarashi, G., & Matsui, K. (2014). Microstructural and bulk property changes in hardened cement paste during the first drying process. *Cement and Concrete Research, 58,* 20–34. https://doi.org/10.1016/j.cemconres.2014.01.007.

Maruyama, I., Ohkubo, T., Haji, T., & Kurihara, R. (2019). Dynamic microstructural evolution of hardened cement paste during first drying monitored by 1 H NMR relaxometry. *Cement and Concrete Research, 122*(August 2018), 107–117. https://doi.org/10.1016/j.cemconres.2019.04.017.

Maruyama, I., & Rymeš, J. (2019). Temperature dependency of short-term length-change and desorption isotherms of matured hardened cement. *Journal of Advanced Concrete Technology, 17*(5), 188–194. https://doi.org/10.3151/jact.17.5.188.

Maruyama, I., Sakamoto, N., Matsui, K., & Igarashi, G. (2017b). Microstructural changes in white Portland cement paste under the first drying process evaluated by WAXS, SAXS, and USAXS. *Cement and Concrete Research, 91,* 24–32. https://doi.org/10.1016/j.cemconres.2016.10.002.

McDonald, P. J., Korb, J. P., Mitchell, J., & Monteilhet, L. (2005). Surface relaxation and chemical exchange in hydrating cement pastes: A two-dimensional NMR relaxation study. *Physical Review E Statistical, Nonlinear, and Soft Matter Physics, 72*(1), 1–9. https://doi.org/10.1103/PhysRevE.72.011409.

Mcdonald, P. J., Mitchell, J., Mulheron, M., Aptaker, P. S., Korb, J.-P., & Monteilhet, L. (2007). Two-dimensional correlation relaxometry studies of cement pastes performed using a new one-sided NMR magnet. *Cement and Concrete Research, 37*(3), 303–309. https://doi.org/10.1016/j.cemconres.2006.01.013.

McDonald, P. J., Rodin, V., & Valori, A. (2010). Characterisation of intra- and inter-C-S-H gel pore water in white cement based on an analysis of NMR signal amplitudes as a function of water content. *Cement and Concrete Research, 40*(12), 1656–1663. https://doi.org/10.1016/j.cemconres.2010.08.003.

Mehta, P. K., & Monteiro, P. J. M. (2006). *Concrete: microstructure, properties, and materials* (3rd ed.). New York: McGraw-Hill.

Mikhail, R.SH, Copeland, L., & Brunauer, S. (1964). Pore structures and surface Areas of hardened Portland Cement Pastes By Nitrogen Adsorption. *Canadian Journal of Chemistry*, *42*, 426–438. www.nrcresearchpress.com

Mikhail, R. S., & Selim, S. A. (1966). Adsorption of organic vapors in relation to the pore structure of hardened Portland cement pastes. *Proceedings of Symposium on Structure of Portland Cemenet Paste and Concrete, 90*, 123–134.

Muller, A. C. A. (2014). Characterization of porosity & C-S-H in cement pastes by 1H NMR. Ecole Polytechnique Federale de Lausanne, Switzerland. Retrieved from https://infoscience.epfl.ch/record/202011/files/EPFL_TH6339.pdf%0A;http://dx.doi.org/10.1016/j.cemconres.2015.04.005

Muller, A. C. A., & Scrivener, K. L. (2017). A reassessment of mercury intrusion porosimetry by comparison with 1H NMR relaxometry. *Cement and Concrete Research, 100*(August), 350–360. https://doi.org/10.1016/j.cemconres.2017.05.024.

Muller, A. C. A., Scrivener, K. L., Gajewicz, A. M., & McDonald, P. J. (2013). Use of bench-top NMR to measure the density, composition and desorption isotherm of C-S-H in cement paste. *Microporous and Mesoporous Materials, 178*, 99–103. https://doi.org/10.1016/j.micromeso.2013.01.032.

Nguyen, H. T., Rahimi-Aghdam, S., & Bažant, Z. P. (2019). Sorption isotherm restricted by multilayer hindered adsorption and its relation to nanopore size distribution. *Journal of the Mechanics and Physics of Solids, 127*, 111–124. https://doi.org/10.1016/j.jmps.2019.03.003.

Nguyen, H., Rahimi-Aghdam, S., & Bažant, Z. P. (2020). Unsaturated nanoporomechanics. *Proceedings of the National Academy of Sciences, 10*, 201919337. https://doi.org/10.1073/pnas.1919337117.

Odler, I. (2003). The BET-specific surface area of hydrated Portland cement and related materials. *Cement and Concrete Research, 33*(12), 2049–2056. https://doi.org/10.1016/S0008-8846(03)00225-4.

Parrott, L. J., Hansen, W., & Berger, R. L. (1980). EFFECT OF FIRST DRYING UPON THE PORE STRUCTURE OF HYDRATED ALITE PASTE L. J. Parrott *, W. Hansen and R. L. Berger Department of Civil and Ceramic Engineering University of l l l i n o i s Urbana, l l l i n o i s 61801 (Communicated by J. P. Skal. *Cement and Concrete Research*, *10*(c), 647–655.

Pearson, D., Allen, A., Windsor, C. G., Alford, N., & Double, D. D. (1983). An investigation on the nature of porosity in hardened cement pastes using small angle neutron scattering. *Journal of Materials Science, 18*(2), 430–438. https://doi.org/10.1007/BF00560632.

Pellenq, R. J. M., & Levitz, P. E. (2002). Capillary condensation in a disordered mesoporous medium: A grand canonical Monte Carlo study. *Molecular Physics, 100*(13), 2059–2077. https://doi.org/10.1080/0026897021012926 5.

Pinson, M. B., Masoero, E., Bonnaud, P. A., Manzano, H., Ji, Q., Yip, S., et al. (2015). Hysteresis from multiscale porosity: modeling water sorption and shrinkage in cement paste. *Physical Review Applied, 3*(6), 64009.

Porod, G., Glatter, O., & Kratky, O. K. O. G. (1982). *Small angle X-ray scattering*. London: Academic Press.

Powers, T. C. (1965). Mechanism of shrinkage and reversible creep of hardened cement paste. In *Proc Int Symp Concr, London, 1965*.

Powers, T. C. (1968). The thermodynamics of volume change and creep. *Matériaux et Constructions, 1*(6), 487–507. https://doi.org/10.1007/BF02473638.

Powers, T., Copeland, L., Hayes, J. C., & Mann, H. M. (1954). Permeablity of Portland Cement Paste. *ACI Journal Proceedings, 51*(11), 285–296. https://doi.org/10.14359/11679.

Richardson, I. G. (1999). Nature of C-S-H in hardened cements. *Cement and Concrete Research, 29*(8), 1131–1147. https://doi.org/10.1016/S0008-8846(99)00168-4.

Richardson, I. G. (2004). Tobermorite/jennite- and tobermorite/calcium hydroxide-based models for the structure of C-S-H: Applicability to hardened pastes of tricalcium silicate, β-dicalcium silicate, Portland cement, and blends of Portland cement with blast-furnace slag, metakaol. *Cement and Concrete Research, 34*(9), 1733–1777. https://doi.org/10.1016/j.cemconres.2004.05.034.

Robens, E., Dabrowski, A., & Kutarov, V. V. (2004). Comments on surface structure analysis by water and nitrogen adsorption. *Journal of Thermal Analysis and Calorimetry, 76*(2), 647–657. https://doi.org/10.1023/B:JTAN.0000028044.44316.ce.

Rymeš, J., & Maruyama, I. (2018). Water vapour sorption isotherms of hardened cement paste at different temperatures. *Proceedings of the Japan Concrete Institute, 40*(1), 45–50.

Sasano, H., Maruyama, I., Nakamura, A., Yamamoto, Y., & Teshigawara, M. (2018). Impact of drying on structural performance of reinforced concrete Shear Walls. *Journal of Advanced Concrete Technology, 16*(5), 210–232. https://doi.org/10.3151/jact.16.210.

Scherer, G. W. (1999). Crystallization in pores. *Cement and Concrete Research, 29*(8), 1347–1358. https://doi.org/10.1016/S0008-8846(99)00002-2.

Scherer, G. W. (2004). Stress from crystallization of salt. *Cement and Concrete Research, 34*(9), 1613–1624. https://doi.org/10.1016/j.cemconres.2003.12.034.

Schreiner, L. J., Mactavish, J. C., Miljkovic, L., Pintar, M. M., Blinc, R., Lahajnar, G., et al. (1985). NMR line shape-spin-lattice relaxation correlation study of Portland cement hydration. *Journal of the American Ceramic Society, 68*(1), 10–16. https://doi.org/10.1111/j.1151-2916.1985.tb15243.x.

Scrivener, K. L. (1989). The use of backscattered electron microscopy and image analysis to study the porosity of cement paste. *MRS Proceedings, 137*, 129–140.

Scrivener, K. L. (2004). Backscattered electron imaging of cementitious microstructures: Understanding and quantification. *Cement & Concrete Composites, 26*(8), 935–945. https://doi.org/10.1016/j.cemconcomp.2004.02.029.

Scrivener, K., Snellings, R., & Lothenbach, B. (2016). *A practical guide to microstructural analysis of cementitious materials*. Boca Raton: Crc Press.

Shi, D., & Winslow, D. N. (1985). Contact angle and damage during mercury intrusion into cement paste. *Cement and Concrete Research, 15*(4), 645–654. https://doi.org/10.1016/0008-8846(85)90064-X.

Sugimoto, H., Kurihara, R., Rymes, J., & Maruyama, I. (2017). A study on the effect of hydration stoppage and pretreatment methods on sorption isotherm white cement paste. In *Japanese Concrete Institute*.

Taylor, H. F. W. (1997). Cement chemistry. *Cement chemistry*. https://doi.org/10.1680/cc.25929.

Taylor, H. F. W., & Turner, A. B. (1987). Reactions of tricalcium silicate paste with organic liquids. *Cement and Concrete Research, 17*(4), 613–623.

Tennis, P. D., & Jennings, H. M. (2000). A model for two types of calcium silicate hydrate in the microstructure of Portland cement pastes. *Cement and Concrete Research, 30*(6), 855–863.

Thomas, M. D. A. (1989). The suitability of solvent exchange techniques for studying the pore structure of hardened cement paste. *Advances in Cement Research, 2*(5), 29–34. https://doi.org/10.1680/adcr.1989.2.5.29.

Thomas, J. J., Jennings, H. M., & Allen, A. J. (1998). The surface area of cement paste as measured by neutron: Evidence for two C–S–H morphologies. *Cement and Concrete Research, 28*(6), 897–905.

Thomas, J. J., Jennings, H. M., & Allen, A. J. (1999). The surface area of hardened cement paste as measured by various techniques. *Concrete Science and Engineering, 1*(March), 45–64. https://doi.org/10.1016/S0008-8846(98)00049-0.

Timmermann, E. O. (2003). Multilayer sorption parameters: BET or GAB values? *Colloids and Surfaces A: Physicochemical and Engineering Aspects, 220*(1–3), 235–260. https://doi.org/10.1016/S0927-7757(03)00059-1.

Tombari, E., Salvetti, G., Ferrari, C., & Johari, G. P. (2005). Thermodynamic functions of water and ice confined to 2 nm radius pores. *Journal of Chemical Physics. doi, 10*(1063/1), 1862244.

Valckenborg, R. M. E., Pel, L., Hazrati, K., Kopinga, K., & Marchand, J. (2001). Pore water distribution in mortar during drying as determined by NMR. *Materials and Structures/Materiaux et Constructions, 34*(244), 599–604. https://doi.org/10.1617/13586.

Valori, A., McDonald, P. J., & Scrivener, K. L. (2013). The morphology of C-S-H: Lessons from 1H nuclear magnetic resonance relaxometry. *Cement and Concrete Research, 49*, 65–81. https://doi.org/10.1016/j.cemconres.2013.03.011.

Valori, A., Rodin, V., & McDonald, P. J. (2010). On the interpretation of 1H 2-dimensional NMR relaxation exchange spectra in cements: Is there exchange between pores with two characteristic sizes or

Fe3+concentrations? *Cement and Concrete Research, 40*(9), 1375–1377. https://doi.org/10.1016/j.cemconres.2010.03.022.

Van Brakel, J., Modry, S., & Svata, M. (1981). Mercury Porosimetery: State of the Art. *Powder Technology, 29,* 1–12. https://doi.org/10.1016/S0422-9894(08)70338-6.

Vidick, B. (1987). Specific surface area determination by gas adsorption: Influence of the adsorbate. *Cement and Concrete Research, 17*(5), 845–847. https://doi.org/10.1016/0008-8846(87)90047-0.

Wang, H., Hellmich, C., Yuan, Y., Mang, H., & Pichler, B. (2018). May reversible water uptake/release by hydrates explain the thermal expansion of cement paste?—Arguments from an inverse multiscale analysis. *Cement and Concrete Research, 113*(March), 13–26. https://doi.org/10.1016/j.cemconres.2018.05.008.

Wang, X., Peng, Y., Wang, J., & Zeng, Q. (2019). Pore structure damages in cement-based materials by mercury intrusion: A non-destructive assessment by X-ray computed tomography. *Materials.* https://doi.org/10.3390/ma12142220.

Wenzel, O., Schwotzer, M., Müller, E., Chakravadhanula, V. S. K., Scherer, T., & Gerdes, A. (2017). Investigating the pore structure of the calcium silicate hydrate phase. *Materials Characterization, 133*(September), 133–137. https://doi.org/10.1016/j.matchar.2017.09.035.

Winslow, D. N., & Diamond, S. (1974). Specific surface of hardened Portland cement paste as determined by small-angle X-ray Scattering. *Journal of the American Ceramic Society, 57*(5), 193–197. https://doi.org/10.1111/j.1151-2916.1974.tb10856.x.

Wittmann, F. H. (1973). Interaction of Hardened Cement Paste and Water. *Journal of the American Ceramic Society, 56*(8), 409–415. https://doi.org/10.1111/j.1151-2916.1973.tb12711.x.

Yio, M. H. N., Mac, M. J., Wong, H. S., & Buenfeld, N. R. (2015). 3D imaging of cement-based materials at submicron resolution by combining laser scanning confocal microscopy with serial sectioning. *Journal of Microscopy, 258*(2), 151–169. https://doi.org/10.1111/jmi.12228.

Yio, M. H. N., Wong, H. S., & Buenfeld, N. R. (2019). 3D pore structure and mass transport properties of blended cementitious materials. *Cement and Concrete Research, 117*(December 2018), 23–37. https://doi.org/10.1016/j.cemconres.2018.12.007.

Zeng, Q., Li, K., Fen-Chong, T., & Dangla, P. (2012). Analysis of pore structure, contact angle and pore entrapment of blended cement pastes from mercury porosimetry data. *Cement & Concrete Composites, 34*(9), 1053–1060. https://doi.org/10.1016/j.cemconcomp.2012.06.005.

Zeng, Q., Wang, X., Yang, P., Wang, J., & Zhou, C. (2019). Tracing mercury entrapment in porous cement paste after mercury intrusion test by X-ray computed tomography and implications for pore structure characterization. *Materials Characterization, 151*(December 2018), 203–215. https://doi.org/10.1016/j.matchar.2019.02.014.

Zeng, Q., Zhang, D., Sun, H., & Li, K. (2014). Characterizing pore structure of cement blend pastes using water vapor sorption analysis. *Materials Characterization, 95,* 72–84. https://doi.org/10.1016/j.matchar.2014.06.007.

Zhang, J., & Scherer, G. W. (2011). Comparison of methods for arresting hydration of cement. *Cement and Concrete Research, 41*(10), 1024–1036. https://doi.org/10.1016/j.cemconres.2011.06.003.

Zhou, Q., & Glasser, F. P. (2001). Thermal stability and decomposition mechanisms of ettringite at < 120°C. *Cement and Concrete Research, 31*(9), 1333–1339. https://doi.org/10.1016/S0008-8846(01)00558-0.

Zhou, C., Ren, F., Zeng, Q., Xiao, L., & Wang, W. (2018). Pore-size resolved water vapor adsorption kinetics of white cement mortars as viewed from proton NMR relaxation. *Cement and Concrete Research, 105,* 31–43. https://doi.org/10.1016/j.cemconres.2017.12.002.

Publisher's Note